Ocean Dynamics (2012) 62:1123–1137
DOI 10.1007/s10236-012-0550-8

High-frequency bottom-pressure and acoustic variations in a sea strait: internal wave turbulence

Hans van Haren

Received: 12 October 2011 / Accepted: 8 May 2012 / Published online: 1 June 2012

Abstract During a period of 3 days, an accurate bottom-pressure sensor and a four-beam acoustic Doppler current profiler (ADCP) were mounted in a bottom frame at 23 m in a narrow sea strait with dominant near-rectilinear tidal currents exceeding 1 ms^{-1} in magnitude. The pressure record distinguishes small and short surface waves, wind- and ferry-induced near-surface turbulence and waves, large turbulent overturns and high-frequency internal waves. Typical low-frequency turbulent motions have amplitudes of 50 N m^{-2} and periods of about 50 s. Such amplitudes are also found in independent estimates of non-hydrostatic pressure using ADCP data, but phase relationships between these data sets are ambiguous probably due to the averaging over the spread of the slanted acoustic beams. ADCP's echo amplitudes that are observed in individual beams show much better phase correspondence with near-bottom pressure, whether they are generated near the surface (mainly air bubbles) or near the bottom (mainly suspended sediment). These 50-s motions are a mix of turbulence and internal waves, but they are not due to surface wave interactions, and they are not directly related to the main tidal flow. Internal waves are supported by stratification varying between extremely strong thin layer and very weak near-homogeneous stratification. They are driven by the main flow over 2-m amplitude sand-wave topography, with typical wavelengths of 150 m.

Keywords Internal waves · Turbulence · Narrow sea strait · Acoustic and pressure observations

Responsible Editor: Jörg-Olaf Wolff

H. van Haren (✉)
Royal Netherlands Institute for Sea Research (NIOZ),
P.O. Box 59, 1790 AB, Den Burg, the Netherlands
e-mail: hans.van.haren@nioz.nl

1 Introduction

Narrow sea straits between two basins can be characterized by strong, mainly oscillatory tidal flows, say larger than 1 m s^{-1}, and large vertical turbulent exchange. The common thought is that the turbulence due to bottom friction is so large that the water column is 'well-mixed' or homogeneous in density from surface to bottom. Such vigorous turbulence may fill the entire water column with material whirled up from the bottom. The largest sizes of these turbulent motions are about 0.9 times the water depth (Nimmo Smith et al. 1999). This turbulence highly depends on the phase of the tidal current and so do stratification, resuspension of material and internal waves.

An example of such a sea strait is the Marsdiep in the Netherlands, connecting the exterior North Sea and the inland tidal flat Wadden Sea, with near-rectilinear tidal currents reaching speeds of 1.2–1.5 ms^{-1}. The North Sea is saltier than the Wadden Sea. In spring, the horizontal density differences are further enhanced by the shallower Wadden Sea warming up quicker than the North Sea. The combination of horizontal density gradient with bottom friction-induced vertically sheared oscillatory tidal flow may set up alternating degrees of stratification, between homogeneous and well stratified, depending on the tidal phase and degree of slip. This 'tidal straining' mechanism was introduced by Simpson et al. (1990) for mid-depth stratification, but it has also been observed in temperature observations very near (<0.5 m from) the bottom (van Haren 2010). Thus, a sea strait, in this case 20–25 m deep with an asymmetric sand-wave bottom varying h=1–2 m in amplitude over wavelengths of typically l=150 m (Sha 1990), may exhibit varying degrees of turbulence, which are generally suppressed by stratification, and internal waves, which are supported by stratification.

Here, we investigate observations in the water column of vertical currents (w) and acoustic echo amplitude (I) to study the differences between turbulent motions, which are expected to dominate during near-homogeneous periods, and internal wave motions, expected to dominate during stratified periods. Both phenomena show relatively large, 0.01- to 0.1-m s^{-1}, vertical motions varying rather rapidly with time as typical periods are between 30 and 100 s. These data are compared with high-resolution bottom-pressure (p) observations, which show a smooth transition from surface wave (SW) to internal wave (IW, including the continuum IWC) bands via infra-gravity waves (IGW). The latter are in part induced by ship-induced turbulent wakes and waves near the surface (van Haren 2009), as well as by frictional bottom turbulence. The more common explanation for IGW reflecting back to open sea is that they follow from wave set-down in the breaker zone at beaches (e.g. Filloux 1980; Webb 1998). As their canonical frequency range [0.002, 0.05] Hz partially includes internal (gravity) waves supported by occasional and local high vertical density stratification and transition to turbulence, this frequency band is more generally named as internal wave turbulence (IWT; van Haren 2011). Here, attention is focused to resolution of these internal, baroclinic hydrostatic and non-hydrostatic contributions to observed near-bottom pressure. Potentially, present-day equipment is capable of measuring such weak pressure variations $O(10–100)$ N m^{-2} or $O(10^{-3}–10^{-2})$ m H_2O (Moum and Smyth 2006).

The data thus constitute a concise combination of bottom-mounted acoustic Doppler current profiler (ADCP) 3-component current, near-bottom echo intensity and temperature [$u(z)$, $v(z)$, $w(z)$, $I(z)$ and T] data and bottom-pressure recorder [p, T] data.

2 Data and methods

Between 28 and 31 May (year days 147 and 150) 2001, a nearly flat 3×1-m bottom frame was moored at 52° 59.025′N, 04° 46.876′E, H=23 m water depth, in the Marsdiep, the 4-km-wide sea strait between the island of Texel and the mainland of the Netherlands (Fig. 1). At the mooring site, the major [tidal] current direction is along the strait axis, about 19° North from East (South from West). The bottom consists of coarse sand, like the outer North Sea to its West and in contrast with finer [resuspendable] sediments in the inner Wadden Sea to its East (Postma 1957; Sha 1990). Weather conditions were favourable, with some moderate westerly winds during the first 2 days and virtually no wind later in the week (Fig. 2a). The Marsdiep is a shielded area, not exposed like the open North Sea or the ocean. As a result, wind

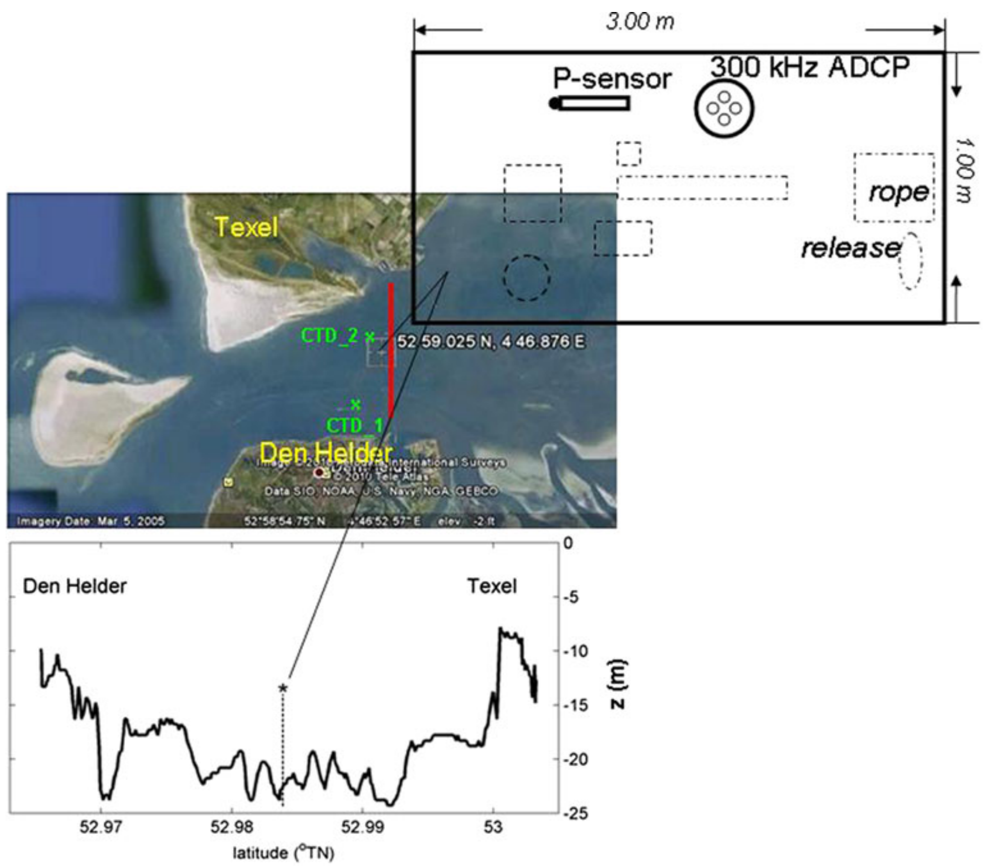

Fig. 1 Mooring frame and Marsdiep (Google Earth) with mooring location (*), two CTD sites (*green x*) and transect (*red line*) with bottom topography (ship-borne ADCP data)

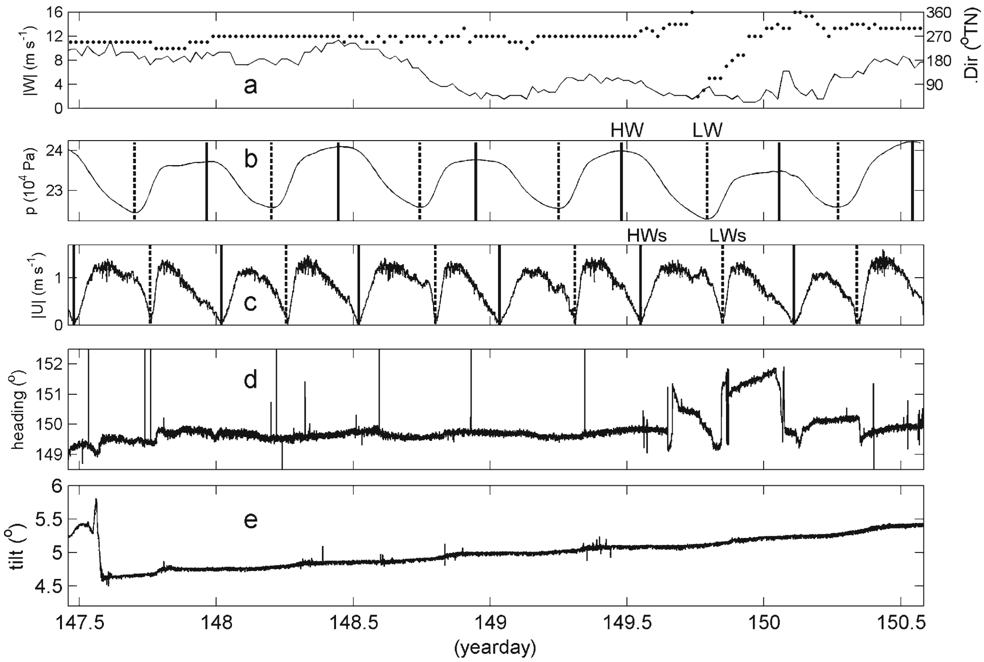

Fig. 2 Time series of **a** wind speed (*solid line*) and direction (*dots*, *scale* to right), measured at Den Helder airport, 7 km to the south of the mooring. **b** Ten-minute averaged bottom pressure, with times of high water (*HW*, *solid line*) and low water (*LW*, *dashed line*) indicated. **c** ADCP current amplitude (measured at 13 m), with times of high water slack (*HWs*, *solid line*) and low water slack (*LWs*, *dashed line*) indicated. **d** ADCP heading (corrected for magnetic declination) and **e** ADCP tilt. Spikes in heading are due to nearby passages of ships, mostly island ferry (van Haren 2009). Time is according to the convention that 1 January 12:00 UTC=0.5 yearday

waves and especially swell are relatively small, <1 m during the period of observations.

The bottom frame was attached via chains and a cable to a second weight about 100 m away that lead to a surface marker. The frame held an upward-looking 300-kHz broadband RDI-ADCP with its acoustic and temperature sensors at 0.42 m above the bottom (mab) and an SBE26 wave & tide (bottom-pressure) recorder with its p and T sensors at 0.08 mab. The ADCP stored single-ping data every 1.85 s, sampling 44 vertical 0.5-m bins. The first bin is 4.0 mab; the transmission length is 1.9 m, resulting in a (single-ping) horizontal current accuracy of 0.09 m s^{-1}. The pressure recorder sampled at 4 Hz (maximum sampling speed), storing 2,000 data points before 100 s rest, every 600 s.

Ship-borne Seabird SBE-911 conductivity–temperature–depth (CTD) observations were made every 1,200 s at two positions: between days 148.20 and 148.35 around low water slack (LWs, 148.25) at position 52° 58.398′N, 04° 46.326′E (CTD_1; Fig. 1) about 1,300 m SSW of the mooring and between days 148.36 and 148.75 around high water slack (HWs, 148.51) at position 52° 59.187′N, 04° 46.687′E about 400 m NW of the mooring. The ship had to change position, because the anchor could not be held at the first location. The CTD data were processed in 0.25-m vertical bins, starting at 1.5–2.5 m from the surface and extending to 1–1.5 m from the bottom. Times of high/low water (HW/LW) preceded HWs/LWs by on average 1.5 h (Fig. 2b, c).

The ADCP's echo intensity I is a measure for acoustic backscatter, which for a 300-kHz ADCP is sensitive to particles of a few millimetres and larger (RDI 1996). This includes suspended sediment, zooplankton and also air bubbles. To quantify raw $I(z)$ in terms of suspended material, it needs corrections for sound attenuation (RDI 1996) and for 'stratified turbulence' due to directional scattering (Merckelbach 2006). In its simplest form, the correction is made by subtraction of its time mean $<I_i>(z)$ from the raw data per depth level z: $dI_i=I_i-<I_i>$, $i=1,\ldots,4$ beam numbers. These data are measured within each of the four, 1°-spreading beams and thus represent a much narrower horizontal area $O(1)$-m^2 estimate than for the current estimates. As a result, variations in echo arrival between the beams (Appendix 1) can be used not only for estimating phase speeds of 'waves' passing, but also to warn for potential erroneous current estimates. The latter are composed of averages between the four beams, that is over the θ=20°-slanted beam spread and thus representing $O(100)$-m^2 estimates. This beam averaging is of some concern when studying small-scale phenomena like 20-m large turbulent patches in areas like the Marsdiep (see Appendix 2).

The discrepancy between estimates averaged over the beam width $O(1)\mathrm{m}^2$ and the beam spread $O(100)\mathrm{m}^2$ is also relevant for estimates of turbulence parameters like Reynolds stresses τ_x, τ_y and turbulent kinetic energy (TKE) production P. As outlined by Lohrmann et al. (1990) for a pulse-to-pulse coherent, 'single-ping' sampling four-beam Doppler current profiler fixed at the sea bed, Reynolds stresses can be estimated by suitable subtraction of variances of Doppler velocities b_i, $i=1,\ldots,4$ within the beams,

$$\tau_x = \frac{\overline{\widehat{b_2'^2}} - \overline{\widehat{b_1'^2}}}{2\sin 2\theta} \equiv -\overline{u'w'};\ \tau_y = \frac{\overline{\widehat{b_4'^2}} - \overline{\widehat{b_3'^2}}}{2\sin 2\theta} \equiv -\overline{v'w'}, \qquad (1)$$

where the prime denotes fluctuating quantity over a suitable mean (overbar) and the hat a measured quantity. The variances are obtained within each of the individual beam (width)s and the estimates (1) constitute averages of the statistics over the beam spread, rather than covariances between beam averaged currents, that is: in general $\tau_x \neq -\overline{\widehat{u}'\widehat{w}'}$, similar for τ_y. This implies that turbulence parameters are estimated over distances $O(1)$m that are expected to resolve the largest turbulent eddies in the Marsdiep.

The variance method is portable to incoherent ADCPs, whether narrow- or broadband, but only when single-ping data are stored and only when the instrument is rigidly fixed in space. In other cases, one is forced to use the Cartesian $[\widehat{u}, \widehat{v}, \widehat{w}]$ data as vector averaging and correction for instrumental tilt and heading cannot be done in the non-Cartesian beam velocity coordinates. Every standard ADCP internally transfers to Cartesian coordinates when two or more pings are to be averaged in an ensemble, regardless of the requested output coordinates.

However, estimates (1) can still be made as averages of statistics over the beam spread, when: (a) all four beams are used and (b) the redundant, so-called 'error velocity' e is scaled like w during post-processing by dividing by $4\cos\theta$ (until to date, this is not done intrinsically). Then, it may be shown (van Haren et al. 1994) that (1) is exactly equivalent to,

$$\begin{aligned} &\overline{\tau_{x'}} = -\overline{\widehat{u}'\widehat{w}'_m}; \overline{\tau_{y'}} = -\overline{\widehat{v}'\widehat{w}'_p}, \\ &\widehat{w}_m = \widehat{w} - \widehat{e}; \widehat{w}_p = \widehat{w} + \widehat{e}, \end{aligned} \tag{2}$$

which is thus not a direct correlation but a variance method. The method still works fine for a slowly rotating instrument, over heading angle φ_1 without correlation with velocity fluctuations, and for which corrections are given in measured parameters $[\hat{u}, \hat{v}, \hat{w}, \hat{e}]$ (van Haren et al. 1994). However, for a tilted system over pitch (φ_2) and roll (φ_3) angles corrections are partially expressed in unknown 'true' velocities $[u, v, w, e]$ (Lohrmann et al. 1990), and only estimates of their size can be given. The combined corrected version of (2) read, for small tilt angles and no correlations between rotation angles and velocity fluctuations, to first order approximation (van Haren et al. 1994),

$$\begin{aligned} &\overline{\tau_{x'}} = -\overline{\widehat{u}'\widehat{w}'_m} - \overline{2\widehat{e}' \sin(\varphi_1)(\widehat{u}' \sin(\varphi_1) + \widehat{v}' \cos(\varphi_1))} - \varphi_2\overline{\widehat{u}'v'} + \varphi_3(\overline{u'\widehat{u}'} - \overline{w'\widehat{w}'_m}), \\ &\overline{\tau_{y'}} = -\overline{\widehat{v}'\widehat{w}'_p} - \overline{2\widehat{e}' \sin(\phi_1)(\widehat{u}' \cos(\varphi_1) - \widehat{v}' \sin(\varphi_1))} - \varphi_3(\overline{v'\widehat{v}'} - \overline{w'\widehat{w}'_p}) + \varphi_2\overline{u'\widehat{v}'}, \end{aligned} \tag{3}$$

in which the 'true' velocities can only be guessed. A first guess are the measured values, which point out that a tilted system will bias especially through the variance terms for anisotropic 'turbulence'. The ADCP's instrument-motion sensors showed that the present mooring was on a 4.7° [sandwave] slope, slowly (at a rate of $0.1°\,\mathrm{day}^{-1}$) becoming more inclined to the vertical (Fig. 2e), probably due to sand washing under the frame by the current. We will use the local coordinates $[x, y, z]$=[along-channel, cross-channel, gravity].

Statistical significance for the estimates (3) is obtained by comparison with distributions made up of repeated computations using randomly shifted series of fluctuating observables, with exclusion of a zone of lags up to 15 s away from zero lag for which the auto-covariance function was exceeding the criterion of 0.05 (see van Haren et al. 1994 for details).

The stresses (3) will be compared with mean shear, to obtain estimates of average (~constant) eddy viscosity A by computing mean stress over mean shear,

$$A_x = \overline{\tau_{x'}} / \left(\partial\overline{\overline{u}}/\partial z\right); A_y = \overline{\tau_{y'}} / \left(\partial\overline{\overline{v}}/\partial z\right), \tag{4}$$

Equations (3) and (4) will be computed for two bands of fluctuating signals, IWC and IWT, for which the filter bounds will be specified in Section 3. 'Turbulent' kinetic energy production P is computed for three different components: a mean, a low frequency including tidal internal wave band, IWC,

$$\begin{aligned} &P_x = \overline{\tau_{x'}}\frac{\partial\overline{\widehat{u}}}{\partial z} + \overline{\tau_{x''}}\frac{\partial\overline{\widehat{u}}}{\partial z} + <\tau_{x''}> \frac{\partial(<\widehat{u}> - \overline{\widehat{u}})}{\partial z} + <<\tau_{x''}>> \frac{\partial(<<\widehat{u}>> - <\widehat{u}> - \overline{\widehat{u}})}{\partial z}, \\ &P_y = \underset{(a1)}{\overline{\tau_{y'}}\frac{\partial\overline{\widehat{v}}}{\partial z}} + \underset{(a2)}{\overline{\tau_{y''}}\frac{\partial\overline{\widehat{v}}}{\partial z}} + \underset{(b)}{<\tau_{y''}> \frac{\partial(<\widehat{v}> - \overline{\widehat{v}})}{\partial z}} + \underset{(c)}{<<\tau_{y''}>> \frac{\partial(<<\widehat{v}>> - <\widehat{v}> - \overline{\widehat{v}})}{\partial z}}, \\ &P = P_x + P_{y,} \end{aligned} \tag{5}$$

in which the prime now indicates fluctuations in the IWC band and <> averaging over the IWC band time scale, <<>> averaging over the IWT band time scale and double-prime fluctuations about this 'mean'. The terms (a) denote the work done by fluctuating IWC (a1) and IWT (a2) motions against mean flow shear, the term (b) work of IWC fluctuations against IWC averaged, mainly tidal, shear and term (c) work of IWT fluctuations against IWC and tidal shear. Turbulence dissipation rate and buoyancy production are not measured.

The bottom-pressure sensor has an absolute accuracy of about 70 Nm^{-2} and a resolution of 8 Nm^{-2} for the 4-Hz sampling rate. SeaBird's accuracy includes temperature compensation of the DigiQuartz sensor, down to about the sensor's resolution. These values are just about adequate to measure non-hydrostatic (vertical velocity accelerations) and internal hydrostatic (baroclinic) pressure variations induced by internal waves, which, moreover, are found at much lower frequencies than the sampling rate of 4 Hz. Moum and Smyth (2006) formulate estimates for bottom-pressure p^{-H} due to internal wave action in terms of current and density variations,

$$p^{-H}(t) = p_{\mathrm{nh}} + p_{\mathrm{ih}} + p_{\mathrm{eh}},$$
$$p_{\mathrm{nh}} = \int_{-H}^{0} \overline{\rho}\frac{Dw}{Dt}d\widetilde{z}; \quad p_{\mathrm{ih}} = \int_{-H}^{0} \rho' g d\widetilde{z}; \quad p_{\mathrm{eh}} = \overline{\rho} g\eta = -\overline{\rho}\int_{-\infty}^{x} \frac{Du^{0}}{Dt}d\widetilde{x} \tag{6}$$

in which p_{eh} denotes the wave's external hydrostatic pressure, p_{ih} internal hydrostatic pressure, p_{nh} non-hydrostatic pressure, ρ density, g acceleration of gravity, η wave-induced sea level variations, superscripts 0 and $-H$ z-positions at surface and bottom, respectively, and $'$ variations around the time mean (overbar). In practice for non-linear waves, the total derivative in p_{nh} can be replaced by the local time derivative: the difference between the two terms due to advection being <10 % (Moum and Smyth 2006). Independently, sea floor pressure can be obtained by integrating the near-bottom horizontal momentum equation,

$$p_{Du/Dt}^{-H}(t) = -\overline{\rho}\int_{-\infty}^{x} \frac{Du^{-H}}{Dt}d\widetilde{x} \approx \overline{\rho}\int_{u^{-H}(t-t_0)}^{u^{-H}(t)} c d\widetilde{u}, \tag{7}$$

in which c denotes a constant phase speed. The transfer from horizontal coordinate to current integral assumes wave propagation without change of form. In practice, integration starts some t_0=500 s before wave arrival (Moum and Smyth 2006).

Due to lack of appropriate simultaneous temperature and salinity measurements that varyingly dominate density variations, p_{ih} cannot be properly computed using the present data. This is unfortunate, because in solitary shelf waves, it appeared the dominant term, equivalent to (7) (Moum and Nash 2008).

The expected values for p^{-H} lie in the range [50, 200]N m^{-2} (Moum and Smyth 2006). In order to measure such small pressure variations in an environment $O(10^5)$N m^{-2}, static pressure requires a stable platform and shielding from dynamic pressure. The well-fixed mooring frame does not vary its tilt more than ±0.2° under vibrations induced by currents apart from a sudden jump in the beginning of the record (Fig. 2e). As a result, the expected pressure errors due to mooring vibrations are smaller than 10 Nm^{-2} in most instances, except during well-identifiable short periods during maximum tidal current and except for the slow trend. The low position of the sensor head at 0.08 mab may result in ~60 Nm^{-2} dynamic pressure at the sensor, if not shielded. For comparison, flows in the interior reach speeds up to 1.4 ms^{-1} (Fig. 2), or 1,000 Nm^{-2} equivalent dynamic pressure.

3 Observations

3.1 Overview

All parameters are dominated by semi-diurnal tidal variations with time (Fig. 3). The relative echo intensity in the upper 5 m varies 180° out of (tidal) phase with that in the remainder of the water column (Fig. 3a). The deeper part also shows a fourth-diurnal component which is absent near the surface. The upper-layer echo intensity is also approximately 180° out of phase with sea level. Maximum near-surface dI occurs during ebb flow (blue in Fig. 3d), when relatively fresh, more turbid Wadden Sea water is advected over North Sea water. Vertical motions (Fig. 3b) are not well observed in this near-surface layer. They are more manifest near the bottom, when near-bottom echoes are large. Larger near-bottom echoes are in general associated with large [tidal] flow speeds that vary fourth-diurnally with time, but also with semi-diurnal varying and periodically very strong near-bottom stratification (Fig. 3c; van Haren 2010). Maximum flood flows are slightly larger than ebb flows, 1.5 and 1.3 ms^{-1}, respectively, but the difference in near-bottom echoes is larger than expected from this difference in current speed alone.

The asymmetry in horizontal flood and ebb flows is partially reflected in tidal vertical motions, which are larger negative (downward) during flood than positive (upward) during ebb. This evidences that the mooring is on a (sand-wave) slope, with its shallow part seaward. It does not imply a bias error in vertical current observations due to improperly corrected instrumental tilt, even though tidal variations are in phase with main horizontal current variations (Fig. 3b and d). Like in historic central North Sea observations, the aspect ratio between vertical and horizontal motions varies with depth, which cannot be attributed to a potential common error in tilt-sensor data. In fact, while the horizontal current amplitude increases towards the surface (Fig. 3d), tidal |w| decreases with distance from the bottom (Fig. 3b). The largest tidal |w| values are observed at 19 m, the lowest level of ADCP observations.

Apart from tidal variations, high-frequency variations are ubiquitous in the vertical motions. Although they also often, but not always as will be shown below, decrease from the lowest level upward, they do not very much depend on the direction of the tidal flow in the sea strait, as they are modulated with fourth-diurnal periodicity. This contrasts with temperature stratification (Fig. 3c), especially very near-bottom temperature stratification, which shows semi-diurnal periodicity, being largest at low water (LW). This, local, near-bottom

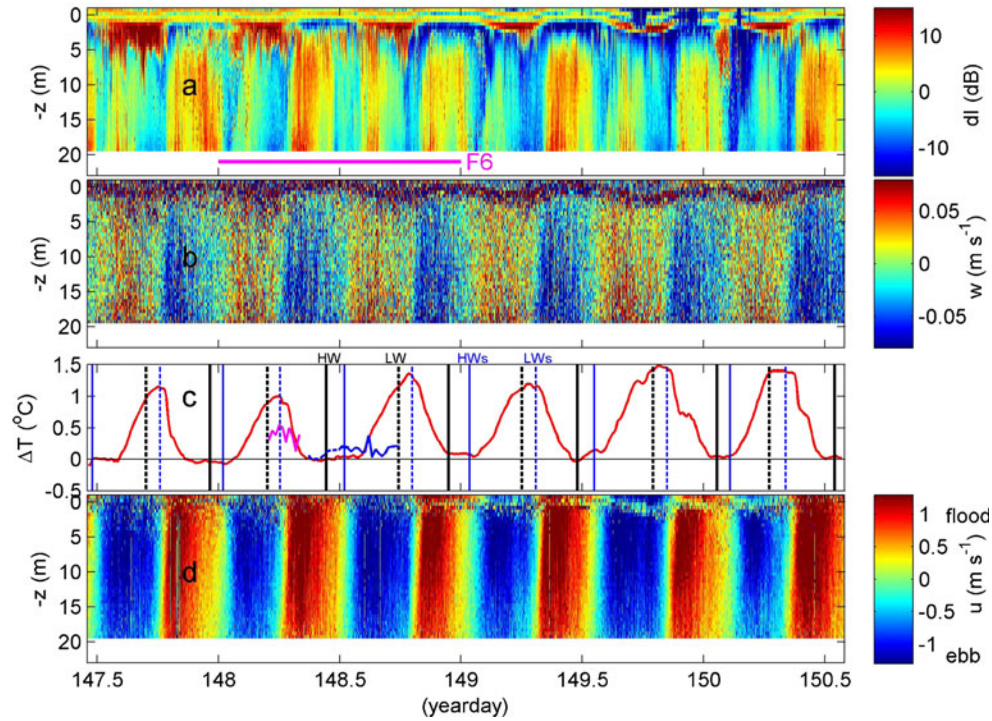

Fig. 3 Overview of 0.54-Hz sampled despiked raw data from bottom-mounted ADCP data in the Marsdiep sea strait. **a** Relative echo intensity of beam 1. Its surface reflection is well visible (double reflection is due to pulse length>bin size) and shows the tidal height variation. The *purple bar* indicates period of Fig. 7. **b** Vertical current averaged over the four beams. The *brown band* indicates bad data due to the direct surface reflection (1.5 m below the actual surface). **c** Vertical temperature difference between moored near-bottom sensors at 0.42 and 0.08 mab (*red*) and between the uppermost (2±1.5 m) and lowest (1.5±0.5 mab) data in CTD profile (*purple*, data 1 km south of mooring, CTD_1 in Fig. 1; *blue*, 450 m northwest of mooring, CTD_2 in Fig. 1). HW/LW indicated in *black*, HWs/LWs in *blue*. **d** East (positive)–west (negative) current component

stratification can be so strong in thin layers that the buoyancy period reduces to $T_N=2\pi/N=50$ s when transferring temperature to density variations and accounting for the North Sea *T–S* relationship $-\delta T/\delta S=-4.5$ (indeed negative) and even down to $T_N=20$ s using the Wadden Sea *T–S* relationship $-\delta T/\delta S=-0.33$ (van Haren 2010). It is unknown how local this stratification is between the sand waves. In the water column, stratification is weaker and, due to cross-estuarine circulation and frontal passages, varies more complex than tidal with time (Fig. 3c). Buoyancy periods are between 200 and 500 s, except during short homogeneous periods. These interior stratification values would mark an upper bound to an IWC band that matches the lower IWT bound (heavy dashed black bar in Fig.4).

However, spectra of vertical motions are nearly flat for frequencies (σ) more than two decades beyond semi-diurnal, well extending into IWT and slightly (that is, non-significantly) increasing up to a sub-maximum around $\sigma=0.03\pm0.01$ Hz before rolling off (Fig. 4a). This confirms the above near-bottom, small-scale estimate of the buoyancy frequency (indicated by a coloured bar at the bottom of Fig. 4c), but are these motions indeed representing internal waves? Provisionally, the band is named IWC_{fs} here, an extension of IWC into IWT and accounting for fine (vertical) scales. For reference, in the upper ocean, high-frequency *W* spectra are near flat over the entire domain between inertial frequency *f* and buoyancy frequency *N* with a weak hump near *N* before rolling off (e.g. Pinkel 1981). These are largely attributed to internal gravity waves, but one could question the linearity of these waves. In contrast, in the ocean interior, internal wave *w* spectra increase much more continuously towards *N* from both low (in the IWC at a rate of σ^{+1}) and high frequencies (van Haren and Gostiaux 2009; also partially visible in Pinkel 1981). Here, the *N* hump is barely visible. Furthermore, its variance varies with little distinction between strong flood and ebb flows and only moderately changes up to $\sigma\approx0.03$ Hz during weak flows. But there are additional observations. It is seen that relative echo intensity varies between different depths, precisely in the $IWC_t=IWC+IWC_{fs}$ band mainly (Fig. 4b). Largest dI are found near the surface, opposite to what is found for *w* in this band (Fig. 4a). Horizontal motions also show a marginally significant roll-off into noise at the frequency of the *w* roll-off, which is found to coincide with an (occasional) roll-off of IWT, or, to be investigated next, IWC_{fs} roll-off (Fig. 4c).

3.2 Some (a)typical pressure observations

The spectra of bottom-pressure ‘*p* spectra’ consist of a high-frequency (acoustic?) short-wave noise part, for frequencies

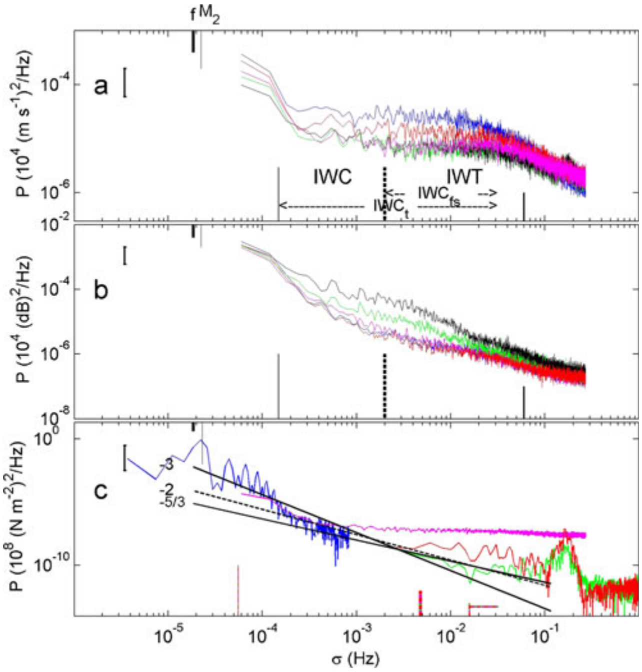

Fig. 4 **a** Moderately smoothed spectra for entire mooring period of w_p at 18.5 (*blue*), 17 (*red*), 12 (*purple*), 9.5 (*green*) and 7 m (*black*). The *black bars* indicate the IWC and IWT bounds based on (minimum, maximum) large-scale interior stratification. **b** As **a** but for relative echo intensity from beam 1. **c** As **a** but for kinetic energy at 13 m (*purple*; multiplied with density instead of mass to have the same units as pressure variance) and 600 s averaged bottom pressure (*blue*). These are compared with bottom-pressure spectra for 500-s periods from days 148.2019 (*red*) and 149.8755 (*green*). The major discrepancy between these two spectra is less IWT variance in the latter. The surface wind-wave (SW) peak around 0.15 Hz is clearly visible for both 500-s periods, as well as in near-surface w_p (black spectrum in **a**). The *coloured bars* indicate small-scale (near-bottom) minimum, mean and maximum N, with a *horizontal bar* attached to the latter indicating the effects of range of Wadden- to North Sea T–S relations. For reference, the *horizontal scale* in periods of time is simply $1/\sigma$ (e.g. 10^{-4}-Hz results in a period of 10^4 s)

σ>0.33 Hz (Fig. 4c). The peak centred around 0.15 Hz represents the hydrostatic surface wind wave (SW) activity. These waves are also seen in near-surface spectra for vertical motions 'w spectra'. Henceforth, we will exclude these motions from our analysis, and we use band-pass filters which have 0.03 Hz as high cut-off, for both vertical current and pressure observations. This cut-off is used, because in oceanic bottom-pressure spectra, a notch is found somewhere between 0.01 and 0.1 Hz (Webb 1998). In the present data, the cut-off also delineates the far end of the fine-scale buoyancy frequency and of IWC_t. In variable form, such spectral notch is found here too, but the rate of decrease from σ<0.01 Hz to the notch, at least σ^{-2}, value and frequency (σ≈0.004–0.01 Hz) of the sub-peak vary considerably (Fig. 4c). Extending the filter cut-off to 0.06 and 0.1 Hz shows a dramatic change in vertical motions, as their spectrum is rather flat in this band (Fig. 4a) and little change in other parameters. As a result, the pressure estimates differ greatly when these extended filter cut-offs are used: into the turbulence range. This is discussed in more detail in Section 3d.

We will use a low-pass filter at σ=0.00015 Hz to denote the lower IWC bound. Henceforth, IWC and IWC_{fs} are considered separately, with a filter at 0.002 Hz approximately at the frequency of change in spectral slope away from −2 in p but no gap in w, or combined as IWC_t. It is noted that these two separate bands exhibit quite different time series and that bottom-pressure bands IWT and IWC_{fs} are indistinguishable at the scale of (Fig. 5).

Time series of bottom-pressure IWT variations (Fig. 5c) that exclude SW and IWC demonstrate a general decrease with time, more or less like the wind speed (Fig. 2a). Additionally, they demonstrate a sudden night-time decrease in variance, which is paradoxically especially visible when the wind is weak, as in the second half of the record (Fig. 5c). The sudden increase in high-frequency IWT following night-time is not associated with high water and precise moment of sunrise, which are 1.5 and 0.7 h prior to the change, respectively, but with timing of daily Texel-ferry passages, that are halted during night-time (Fig. 5d). Thus, presumably, the ferry's wake generates turbulence and, perhaps, 'wave'-motions that cause IWT, extending from the surface down and dominating most of the sea strait on a quasi-permanent basis when the ferry operates. In calm weather, such wakes remain visible at the surface for half an hour, which is the time between crossings. Less likely, such motions are generated due to near-surface heating or wave action, as there is no direct link to a sudden increase nearly an hour after local sunrise. This suggests that besides wind effects, a non-negligible part of the IWT band, between 0.004 and 0.04 Hz, is attributable to artificial, ferry-made motions. The IWC band is more invariant between day- and night-time and shows relatively high values around LW (Fig. 5c). Overall, IWC amplitude shows a 1.5- to 2-day variability of unknown source. Except for weak tidal variations, this is different from u_{IWC}, which shows a more distinct semi-diurnal variability with maxima at LW (Fig. 5a). This contrasts completely with the fourth-diurnal variability in u_{IWT}. Thus, a direct correspondence between p and u is hard to make.

The apparent lack in overall correspondence is on the one hand confirming proper shielding of the pressure sensor. On the other hand, it is yielding a negative result on the (internal) wave description of $p\sim u$ in (7). However, it must be noted that mid-depth currents are plotted in Fig. 5a, and proper near-bottom currents have not been measured. In Section 3.4, we will compare in more detail.

3.3 Reynolds stress estimates

The mid-depth along-channel Reynolds stress estimate of the IWT band (Fig. 5b, black) follows the fourth-diurnal modulation of the along-channel current amplitude in the

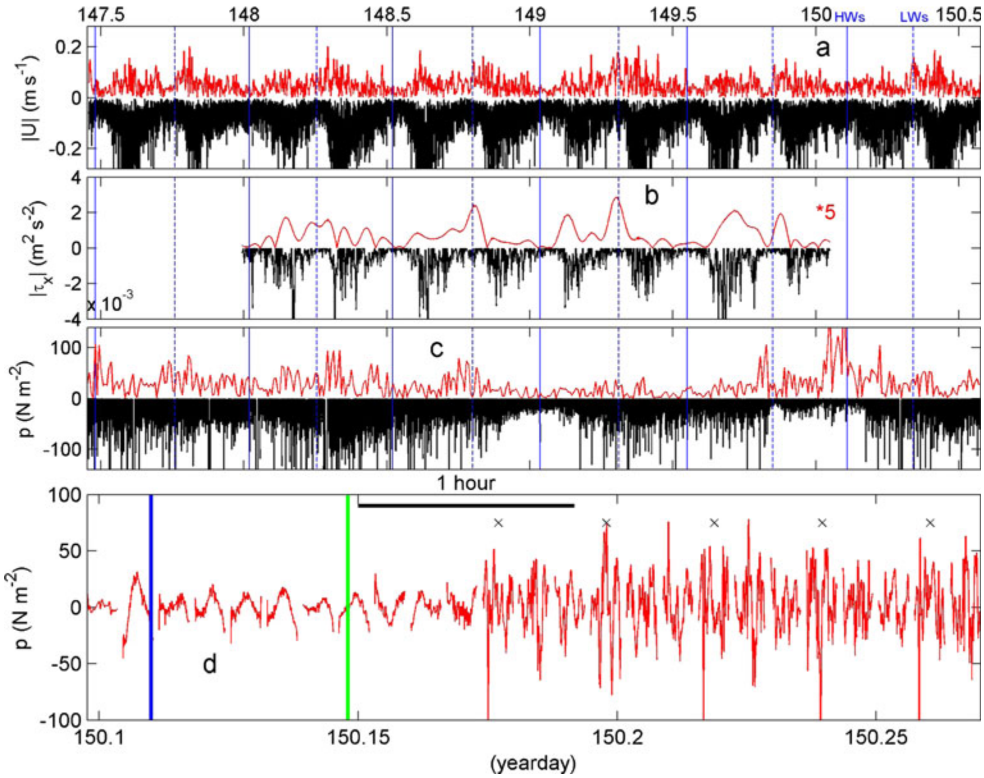

Fig. 5 **a** Time series of current amplitude at 11 m, for IWC (*red*) and IWC_{fs} (~IWT) band (*black*, negative absolute values). **b** Along-channel stress values at 11 m for IWC (*red*, positive absolute) and IWT (*black*, negative absolute). **c** As **a**, but for bottom-pressure observations (including spikes due to ferry passages). **d** Detail of IWC_{fs}/IWT bottom pressure across ferry-time transition on 31 May. The scheduled ferry passages at the latitude of the mooring are indicated by *crosses*. HWs is indicated by the *blue line*, sunrise by the *green line*

same band (Fig. 5a, black). In contrast, the corresponding IWC band portions (red curves) show more of a semi-diurnal variation, with peaks more or less around LWs and weakest values around HWs. This corresponds with p_{IWC} in the first half of the record, but less so in the second half. The corresponding IWT-Reynolds stress estimate shows little correspondence with p_{IWT}. This may have to do with lack of near-bottom ADCP observations, but also point at a larger influence of wind/ferry/bubbles turbulence on bottom pressure.

The above Reynolds stresses suffer from a first principle: one or more clean spectral gaps to separate the signal in two or more portions. Especially in w (Fig. 4a), the spectral separation is rather arbitrary. Nothwithstanding that, the overall values for eddy viscosity show typical results for an estuarine channel like the Marsdiep (Fig. 6a, b). The average IWC values are fairly uniform with depth and are about 0.01 m^2 s^{-1}, whereas the larger IWT value for the along-channel direction steadily increases towards the bottom suggesting large frictional influence. Corresponding average kinetic energy production rates (Fig. 6c) show all positive values, except for near-bottom IWT shear production which apparently feeds energy into the IWC/internal tidal band. This is indeed more or less compensated by IWC production. The mean flow shear production rates are both positive, largest just below mid-depth and in general smaller in values than the shorter-scale production rates (terms (5*b*) and (5*c*) in average form in Fig. 6c).

3.4 Detailed observations

The nearby CTD profiling down to about 1–1.5 mab during the second day of the mooring period shows mid-depth stratification, mainly around LWs (Fig. 7). This stratification is about half the size of the observed near-bottom (temperature) stratification. It is accompanied by near-surface (down to 10 m from the surface) enhanced acoustic echoes and low near-bottom echoes (Fig. 7a). Relative echoes reverse sign about an hour after tidal current direction change, accompanied by and potentially associated with an increase in both IWC (Fig. 7c) and IWT (Fig. 7d) vertical motions. Around LWs, IWC occur, whilst IWT are absent. Around HWs, also IWC are weaker whilst some interior stratification occurs with buoyancy period of about 400 s (see also Fig. 3c). Already 3 h before HWs, near-bottom echoes decrease and only short-lived blobs remain near the surface. These blobs occur between 3 h before and 3 h after HWs in this particular tidal period, but are nearly absent in the remainder of the observational period. This may reflect the precise positioning of a frontal area in the sea strait with respect to the mooring (centre). Like in every tidal period, about 2 h after HWs, the ebb-flow near-surface stratification occurs, which is accompanied by near-bottom echoes during the 2 h of maximum ebb. Below (Figs. 9, 10, 11 and 12), we will discuss three typical examples from this period and an example from night-time high water. Except for one, the examples are for such short duration (400–

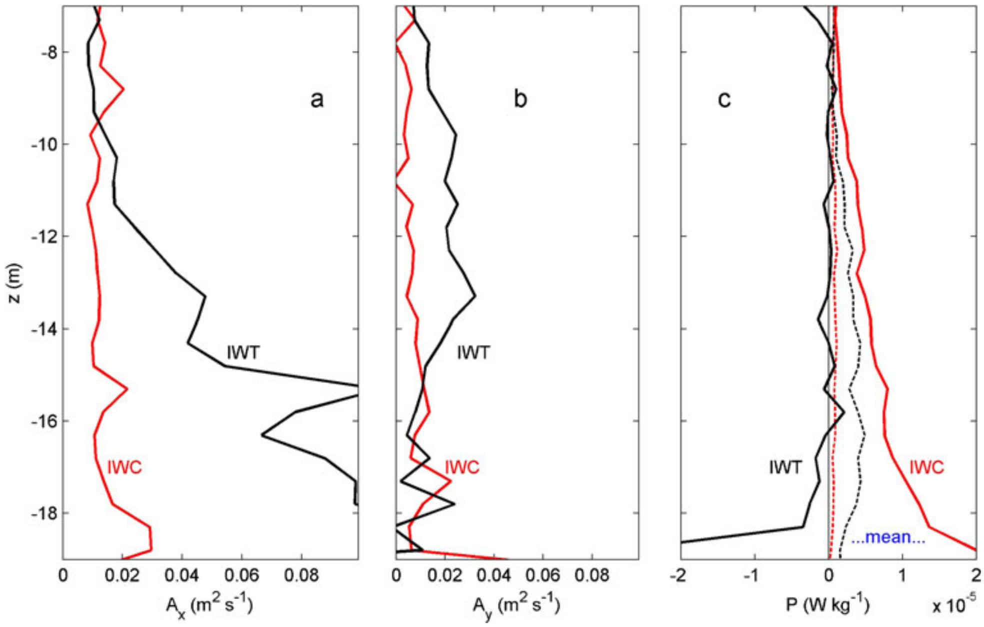

Fig. 6 Two-day average turbulence parameter estimates as a function of depth. **a** Eddy viscosity for along-channel direction using (4). **b** Eddy viscosity for cross-channel direction using (4). **c** Turbulent kinetic energy production using (5) in average form. The *dashed graphs* indicate mean flow shear production, the *solid graphs* fluctuating (tidal/internal wave) current shear production (see text)

600 s) that IWC is not resolved and they are thus incorporated as 'background' in $\mathrm{IWC_{fs}}$/IWT which are investigated.

As noted for mid-depth values in Fig. 5b, the stress estimates for the 1-day period of Fig. 7 are dominated by the tide (Fig. 8). Distinctively, IWC stresses and TKE production show shorter-scale variability than tidal, in both along- and cross-channel directions and more or less independent of depth in the range of observations, and clearly absent around HWs (days 148.02 and 148.55). Noting that the upper 7 m near the surface and the lower 4 m near the bottom are not sampled by the ADCP, these *P* and stress variations are not mimicked by constant viscosity–shear variability, which is much more tidal for the dominant along-channel direction. This dominant tidal variability is also found in IWT shear and, as noted before, also in IWT stress and *P*. Also, note the mainly negative (blue) *P* in IWT, especially near the lower end of the range, when the largest positive (red) values are observed in IWC.

During the largest stratification, the second half of ebb, largest near-surface echoes occur delineating the nearly void interior in terms of acoustic echo (Fig. 9). The near-surface

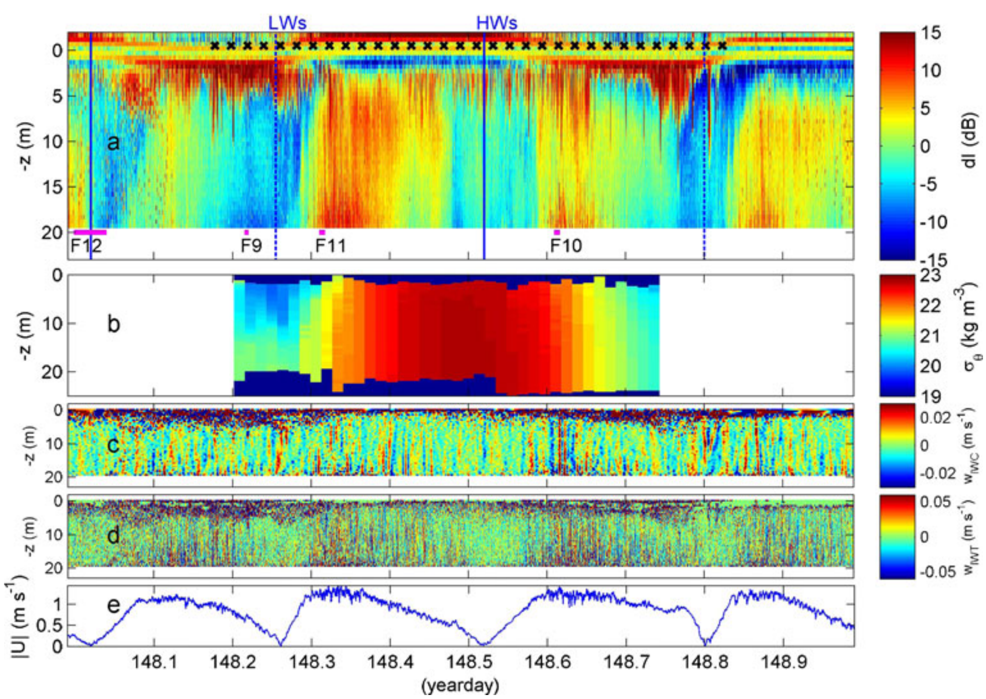

Fig. 7 Detail for 1 day, including the period of CTD observations. **a** Raw relative echo intensity of beam 1. *Crosses* indicate the scheduled passing of the Texel island ferry. **b**. Relative density from ship-borne CTD data referenced to surface. The ship had to be re-positioned at day 148.34, due to much sediment whirling up and anchor slipping. **c** Vertical current, IWC band. **d** As **c**, but for IWT. **e** Current amplitude at 13 m, low-pass filtered <0.01 Hz

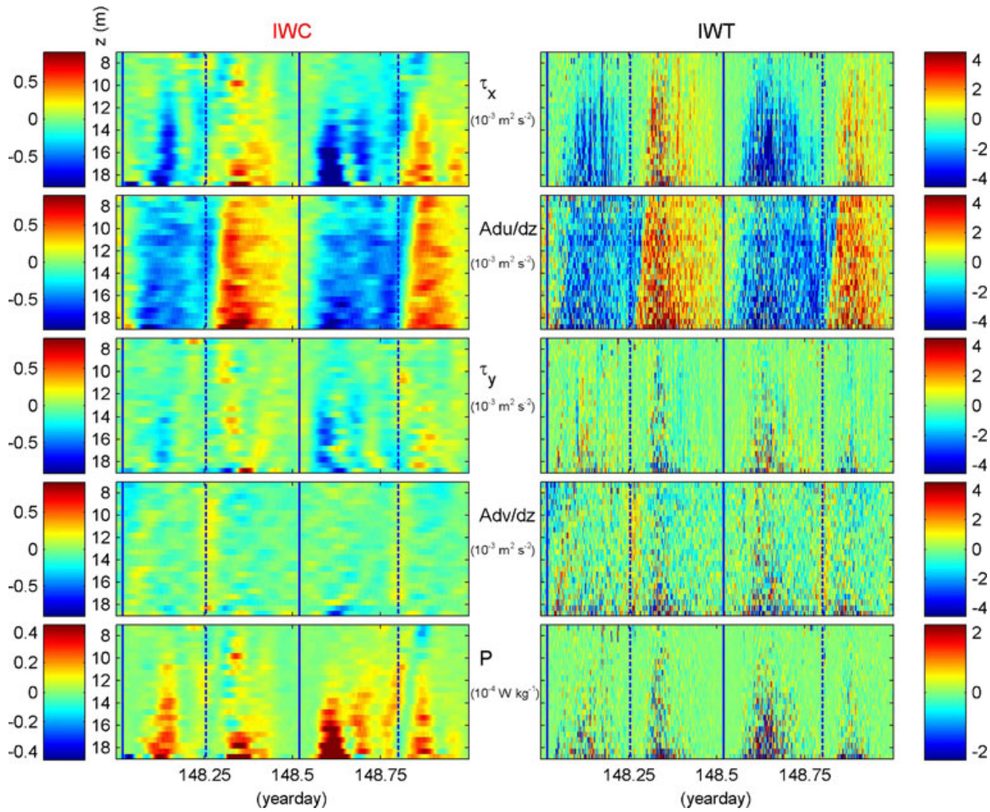

Fig. 8 Turbulence estimates for period of Fig. 6. *Left column* IWC, *right column* IWT band. *Upper two rows* along-channel stress and shear-stress estimate using constant eddy viscosity $A=10^{-2}$ m^{2}s^{-1} for IWC and $A=5\times10^{-2}$ m^{2}s^{-1} for IWT. *Third and fourth rows* ditto, for cross-channel estimates. *Fifth*, lowest, panels are respective turbulence kinetic energy production estimates

echoes reflect air bubbles, induced naturally by passing foam bands due to wind rows or water mass separations. They are clearly distinguishable from more intense bubble clouds induced by ships, notably the island ferry (passing the mooring around day 148.219 in Fig. 9). Ebb flow $U\approx-0.6$ ms^{-1}, and the interface layer between high and low echoes passes the mooring with a periodicity of about 100 s. Smaller-scale variations have typical periods of 10 s. These may correspond with the surface waves, which have a similar periodicity (green curve in Fig. 9c). The IWC$_{fs}$-band bottom-pressure variations (black curve in Fig. 9a, c) have typical amplitudes of about 50 Nm^{-2} and somewhat resemble the depth variation of the near-surface echo interface, with time shifts of about 30 s. Exception is the passage of the ferry, with a typical large dip surrounded by two smaller peaks (van Haren 2009) and possibly another ship passage further away just before day 148.217 showing the same characteristics as the ferry. These passages are not seen in the integrated horizontal momentum Eq. (7) (purple curve in Fig. 9a), which otherwise shows similar amplitudes as observed p, but with ambiguous phase (differences). The ambiguous phase differences may be due to our 'bottom' momentum ADCP data being taken at 4 mab. The ferry passage is also seen in 'non-hydrostatic pressure' signal inferred from integration of the time derivative of vertical current observations (Moum and Smyth 2006) (purple curve in Fig. 9c).

Ideally, integration of p_{nh} term in (6) is across the entire water column, but here, we have to do with good data between $-19<z<-7$ m. This inferred time series shows typical amplitudes that are similar to that of observed bottom pressure, but their correspondence is ambiguous: sometimes in phase, sometimes out of phase. This may have to do with vertical integration over only part of the water column, as we lack the 4 m nearest to the bottom and approximately 7 m near the surface. The observed vertical motions in the remaining centre half show a 40- to 50-s periodicity, mainly in the bottom half (Fig. 9b). They thus seem to be generated close to the bottom, without whirling up sediments, if acoustic echoes reflect these.

Extension of IWC$_{fs}$ to IWT shows a dramatic change in foremost the w and p_{nh} terms (not shown). Not only dominance of high frequency is pertinent, but also associated amplitude increase (about doubling with doubling of filter cut-off). This is only weakly found in bottom pressure and in p_{ih} and $p_{Du/Dt}$ estimates. It suggests that turbulence is most directly affecting vertical motions. Indeed, the w observations like in Fig. 9b resemble in magnitude and variation large eddy simulation (LES)-numerical modelling of stratified turbulence in an estuary under tidal strain (Li et al. 2008). However, the present observations show vertically more coherent w than found in the mainly turbulent LES. Recall that pressure Eqs. (6) and (7) are for internal wave motions, not including turbulence.

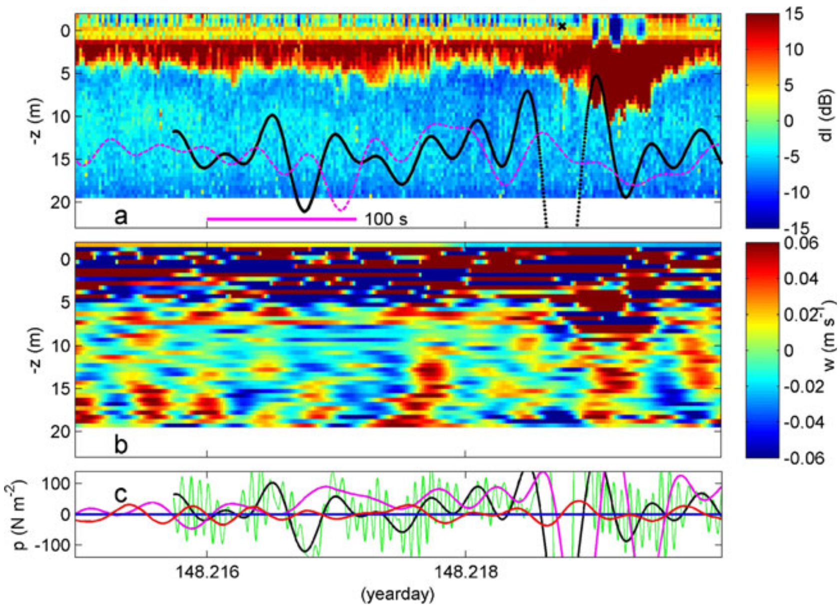

Fig. 9 Detail of 400-s duration during very strongly (near-bottom and interior) stratified and decreasing ebb flow. In Figs. 9, 10, 11 and 12, vertical scales are all the same, but horizontal (time) may vary. **a** Raw relative echo intensity of beam 1. The *cross* indicates the scheduled passing of the Texel island ferry, which induces the large blob of downward-moving echoes (due to air bubbles) shortly after the ferry's passage close to the mooring near day 148.219 (van Haren 2009). Otherwise, the strong echoes reflect near-surface bubble clouds and stratification of fresher, more turbid Wadden Sea over North Sea waters. No 'near-bottom' echoes (from 19 m and up) are observed. The ferry also induces a strong dip in bottom pressure (*black curve*, repetition of curve in **c**; arbitrary scale). The bottom-pressure record is compared with pressure estimated from ADCP data via integration of horizontal near-bottom (4-mab) current (7) (*purple*, using mean current for phase speed, see text; same arbitrary scale as *black curve*). **b** Vertical current, IWC_t, dominated by IWC_{fs} at this time scale. Bad data (*red* or *blue*) are found in the near-surface strong echoes area (cf. a). **c** Bottom pressure filtered for IWC_{fs} (*black*) and for IWT including surface wind waves (*green*). These are compared with pressure estimated using ADCP data: non-hydrostatic pressure in (6) (IWC_{fs}: *red*; IWC: *blue* (negligible)) and pressure due to external surface displacement of internal motions (*purple*). Note the latter showing the large dip attributed to ferry passage also found in bottom pressure, but offset in time by about 15 s

Quite different is a period with weakly stratified, maximum ebb flow ($U \approx -1.3$ ms^{-1}); the largest echoes occur near the surface down to 10 m in small groups 40–70 s apart, but seem to alternate with likewise periodic and almost as intense echoes extending above the bottom up to 10 mab (Fig. 10a). One could interpret this as the advection of convection cells that passed the mooring, with air bubbles being pushed down before and after sediment being whirled up. This is partially reflected in bottom-pressure IWC_{fs} and to similar extent of integrated momentum (7) but at different phase occasionally. Similarity is found at small-scale (~50 s periodicity) and large-scale (~150 s) motions. However, correspondence with integrated vertical motions is harder to grasp, which are dominated by the 50-s motions (Fig. 10c). As before, most intense vertical motions are found in the bottom half of the water column (Fig. 10b), but here, they extend up to the near-surface layer.

A qualitatively similar impression is obtained during the moderately stratified, near-maximum flood flow, $U \approx 1.2$ ms^{-1} (Fig. 11), although two differences are noted. Firstly, the echoes extending from the bottom up are more intense and higher up reaching 5 m or closer to the surface (Fig. 11a). Secondly, vertical motions are more concentrated around mid-depth, rather than at the lowest level of observations 4 mab (Fig. 11b). But like in Fig. 10, dominant periodicity of echo, vertical currents and bottom-pressure variations seem about 50 s. Again, directly observed bottom pressure best resembles periodicity in near-bottom echo variations, but integrated vertical motions p_{nh} in (6) follow nicely, occasionally and sometimes not (Fig. 11c) and likewise do horizontal momentum (7) (Fig. 11a). Amplitudes of the estimated terms match observed bottom pressure.

Large coherent vertical motions are absent during near-homogeneous conditions around HWs (Fig. 12), which especially also contrasts with conditions near LWs (Fig. 9). Associated with some remaining echoes up to mid-depth are weak vertical motions with a periodicity of about 200 s (Fig. 12a, b). For the remainder of the period in Fig. 12, coherent vertical motions are not distinguishable. The pressure record also shows small amplitudes and, especially after HWs, only high-frequency IWC_{fs} variations with time. The amplitude of non-hydrostatic pressure has a standard deviation of 15 Nm^{-2}, which is about 1.5 times the estimated noise level (Fig. 12c).

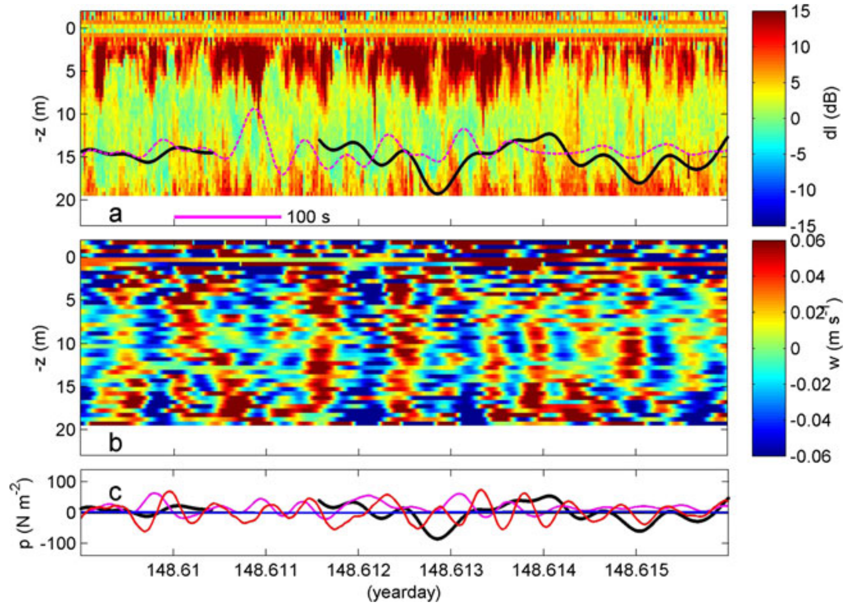

Fig. 10 As Fig. 9, but for 600 s during moderate stratification (using Wadden Sea *T*–*S* relationship, the buoyancy period reaches down to 50 s) under near-maximum ebb flow. In **c**, no surface wind waves are given. In **a** and **c**, the purple curves are computed using a constant phase speed of $c = -0.1$ m s^{-1}, instead of the ten-fold larger mean current speed

4 Discussion

The predominant 50±20-s variations in directly observed bottom pressure fall within the IWC_{fs}/IWT range. In this narrow and relatively shallow sea strait, however, they unlikely result from surface wave set-up or interaction in the breaker zone (Longuet-Higgins and Stewart 1964); as such, long waves are expected to reflect into the open sea. There are several additional observations that suggest a predominance of turbulent and internal wave motions over possible non-linear waves in the observed IWC_{fs}/IWT band.

The additional observations are not perfect, as detailed density depth–time series are lacking and useful ADCP data are only between $-19 < z < -7$ m whilst horizontal beam spread averaging across 10±7 m barely resolves turbulence scales of which the largest are expected to be ~20 m. Nonetheless, estimates of several terms in the (non)linear internal wave pressure Eqs. (6) and (7) show similar magnitude and occasional comparable phases as observed bottom pressure. Firm overall correspondence is lacking, but this can hardly be anticipated considering the above shortcomings. Long nonlinear solitary waves as observed by Moum and Nash (2008) are not clearly found in the present record. The observed and estimated 'bottom' pressure are dominated by *O*(10–100) N m^{-2} variations that are much more permanent in apparition, with a diurnal but a weak semi-diurnal variation with time.

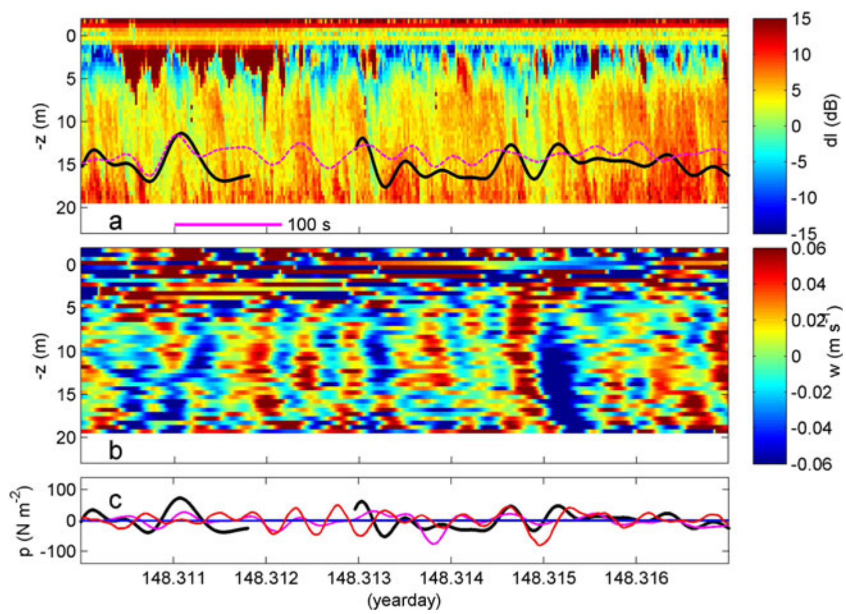

Fig. 11 As Fig. 10, but for 600 s during fairly strongly stratified near-maximum flood flow

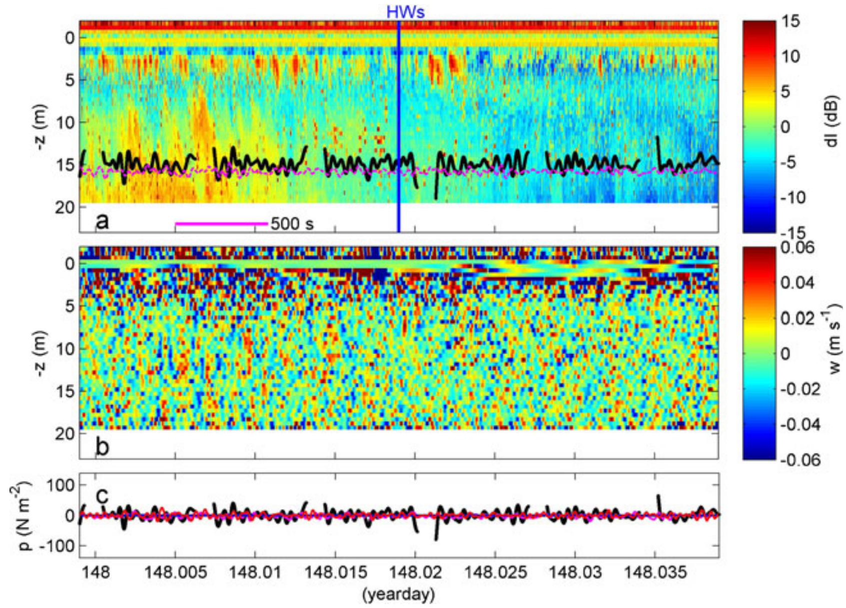

Fig. 12 As Fig. 10, but for 3,500 s (~1 h) during near homogeneity around HWs and using c=0.1 ms^{-1}

After comparison with ADCP's echo and vertical current observations, it is demonstrated that the diurnal variations are in part due to bubble clouds injected by wind and by ferry crossings. In general, turbulent near-surface layers and turbulent sediment resuspension near the bottom, as evidenced in echoes, correspond very well with IWC$_{fs}$/IWT pressure variations. To a lesser extent, but dominated at the same short-term periodicity of ~50 s, vertical motions concentrated in the lower half of the water column accompany the echo and pressure variations. The motions could be turbulent overturns that are characterized by a horizontal length scale of 0.9 H≈20 m (Nimmo Smith et al. 1999). They could also manifest internal waves, as near-bottom stratification can be sufficiently large to support them. The latter are favoured here, as most high-frequency vertical motions have the largest amplitudes at the lowest observational level, where also stratification is strongest. As for generation mechanism, interaction with the tidal flow and the sand waves seems most likely. It is unclear whether such lee-wave generation induces the 50-s periodic motions as free internal waves or as turbulent eddies that are locked to the 150-m-long sand-wave bars. Supposedly, the near-surface bubble clouds and turbulence become modified by internal waves. A firm correlation is not found between IWC$_{fs}$ motions' periodicity and downward tidal flow speeds. The present observations nonetheless suggest a coupling between IWC and IWT or a continuation of IWC into the IWT band: IWC$_{fs}$. The IWC observations of mid-depth amplitude maximum in w and bottom-pressure amplitude tidal modulation with maxima around LWs leave no doubt about this frequency band being dominated by internal waves.

The precise characterization of the high-frequency, short-period IWT band motions requires further detailing of dedicated observations, including detailed depth–time density observations and near-bottom current measurements. It would be good to perform such observations at several closely (<100-m horizontal spacing) moored locations.

Acknowledgments I thank the crew of the R/V Navicula for assistance. Theo Hillebrand and NIOZ-MTM prepared the instrumentation and the mooring frame.

Appendix 1

ADCP beam spread variations and potential errors: echo intensity

Echo intensity is measured in each of the four beams individually. As a result, arrivals of distinct phenomena can be used for estimating advective phase speeds of structures passing. From the heading information of Marsdiep's ADCP (Fig. 2d), it is known that beam 3 was only 11° to the East of the cross-channel axis, so that the main current is more or less in the direction of beams 1 (pointing to the North Sea) and 2 (pointing to the Wadden Sea). This is indeed clearly visible in echoes between the beams, for example during flood (Fig. 13). Naturally, the non-simultaneous arrival of structures smaller than the beam spread has its impact on current estimates which are averaged over the (four) beam spread (Appendix 2).

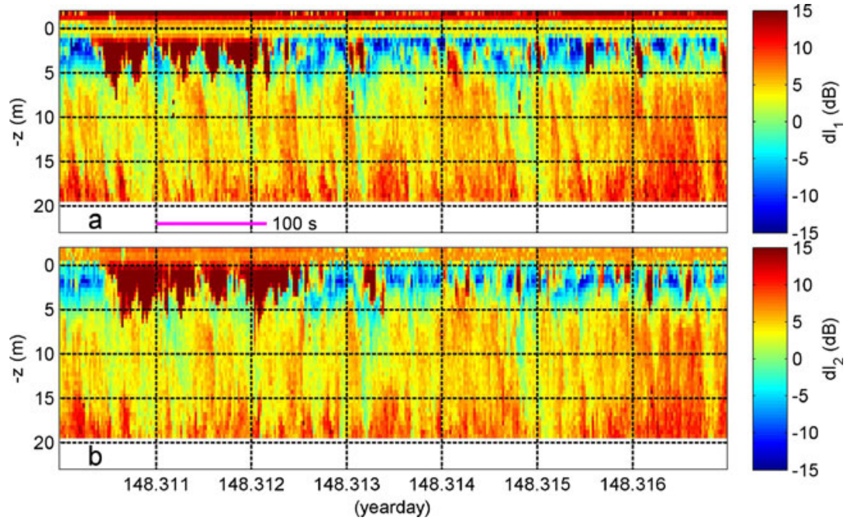

Fig. 13 Comparison between relative echo intensity measured in beams 1 (**a**) and 2 (**b**) during a 600-s period of near-maximum flood flow (same as Fig. 11). Clearly, beam 1 is hit first, near the surface about 15 s before beam 2, and providing a more slanted pattern as expected for flood advection at a speed of 1.2 ms^{-1} for beams pointing into (beam 1) and with (beam 2) the current

Appendix 2

ADCP beam spread variations and potential errors: current estimates

In an area like the Marsdiep, where small-scale topography and turbulent eddies O(10 m) can dominate flow conditions, one can expect current variations or inhomogeneities being differently measured in ADCP's vertically slanted acoustic beams that are separated horizontally over the same distance. An adequate means to verify potential errors due to averaging ADCP's current estimates over the beam spread is verification using the redundant fourth beam the contribution of [horizontal] current inhomogeneities $\Delta u_{ij}=u_i-u_j$, similar for Δv_{ij}, $i\neq j$ different beam numbers. After all, the definition of the vertical current average of the four beams reads:

$$w=\sum_{i=1}^{4}-b_i/4\cos\theta=\sum_{i=1}^{4}w_i/4+(u_1-u_2)\cos\theta/4 +(v_3-v_4)\cos\theta/4,$$

where b_i denotes the truly measured velocities in the direction of each of the beams. The indexed current components are given in instrumental coordinates, as if beam 3 is pointing to the north. The fourth beam is invoked when considering the properly scaled (van Haren et al. 1994) subtraction of two beam pairs, the 'error velocity':

$$e=\sum_{i=1}^{2}b_i/4\cos\theta-\sum_{i=3}^{4}b_i/4\cos\theta=\sum_{i=1}^{2}-w_i/4+\sum_{i=3}^{4}w_i/4 -(u_1-u_2)\cos\theta/4+(v_3-v_4)\cos\theta/4.$$

As indicated by van Haren et al. (1994), addition $w_{\mathrm{p}}\equiv w+e$ and subtraction $w_{\mathrm{m}}\equiv w-e$ isolate potential horizontal

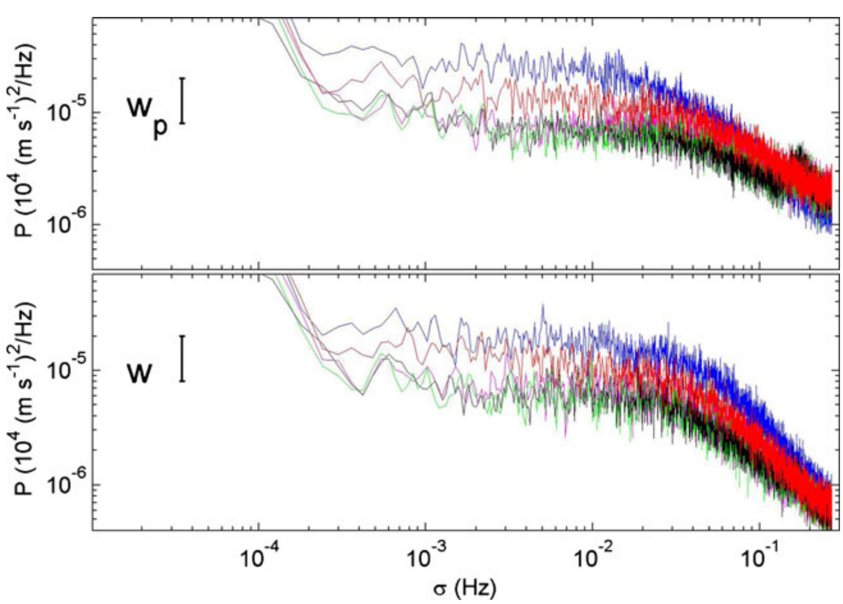

Fig. 14 Enlargement of Fig. 4a, compared with original four-beam w at the same depths

current inhomogeneity effects on vertical current estimates to its u and v components, respectively.

As the main current is more or less in the direction of beams 1 and 2 (Appendix 1), w_p predominantly captures along-channel current inhomogeneities, which we expect to be the more vigorous if any directionality in overturning and short-scales waves occurs. Van Haren et al. (1994) found that near a sloping bottom, variations in the along-slope current component caused a measurable defect in observed w. Here, we see some differences in high-frequency w and w_p amounting up to 20 % in variance (Fig. 14).

Of some other concern in w observations is potential bias in tilt-sensor data, which may incorrectly transfer horizontal current data in w despite the internal correction for each individual acoustic measurement ping. According to the manufacturer, tilt should be measured better than ±0.5°. Here, its bias error is verified at the tidal frequency. Over time, tilt varies slowly by about 0.5° (Fig. 2e), but no measurable effects on w are found, not at semi-diurnal tidal frequencies, which are thus genuinely measured and are due to up/down motions over the sand waves, and certainly not at the much larger aspect ratio high-frequency IWT, which are definitely genuine.

References

Filloux JH (1980) Pressure fluctuations on the open-ocean floor over a broad frequency range: new program and early results. J Phys Oceanogr 10:1959–1971

Li M, Trowbridge J, Geyer R (2008) Asymmetric tidal mixing due to the horizontal density gradient. J Phys Oceanogr 38:418–434

Lohrmann A, Hackett B, Røed LP (1990) High resolution measurements of turbulence, velocity and stress using a pulse-to-pulse coherent sonar. J Atmos Ocean Tech 7:19–37

Longuet-Higgins MS, Stewart RW (1964) Radiation stress in water waves: a physical discussion, with applications. Deep-Sea Res 11:529–562

Merckelbach LM (2006) A model for high-frequency acoustic Doppler current profiler backscatter from suspended sediment in strong currents. Cont Shelf Res 26:1316–1335

Moum JN, Nash JD (2008) Seafloor pressure measurements of nonlinear internal waves. J Phys Oceanogr 38:481–491

Moum JN, Smyth WD (2006) The pressure disturbance of a nonlinear internal wave train. J Fluid Mech 558:153–177

Nimmo Smith WAM, Thorpe SA, Graham A (1999) Surface effects of bottom-generated turbulence in a shallow tidal sea. Nature 400:251–254

Pinkel R (1981) Observations of the near-surface internal wave field. J Phys Oceanogr 11:1248–1257

Postma H (1957) Size frequency distribution of sands in the Dutch Wadden Sea. Arch Néerl Zool 12:319–349

RDI (1996) Acoustic doppler current profiler, principles of operation, a practical primer. RDI, San Diego

Sha LP (1990) Surface sediments and sequence models in the ebb-tidal delta of Texel inlet, Wadden Sea, the Netherlands. Sed Geol 68:125–141

Simpson JH, Brown J, Matthews J, Allen G (1990) Tidal straining, density currents, and stirring in the control of estuarine stratification. Estuaries 13:125–132

van Haren H (2009) Ship-induced effects on bottom-mounted acoustic current meters in shallow seas. Cont Shelf Res 29:1809–1814

van Haren H (2010) Very near-bottom tidal straining in a sea strait. Geophys Res Lett 37:L16603. doi:10.1029/2010GL044186

van Haren H (2011) Internal wave-turbulence pressure above sloping sea bottoms. J Geophys Res 116:C12004. doi:10.1029/2011JC007085

van Haren H, Gostiaux L (2009) High-resolution open-ocean temperature spectra. J Geophys Res 114:C05005. doi:10.1029/2008JC004967

van Haren H, Oakey N, Garrett C (1994) Measurements of internal wave band eddy fluxes above a sloping bottom. J Mar Res 52:909–946

Webb SC (1998) Broadband seismology and noise under the ocean. Rev Geophys 36:105–142